Article

Tectonic Setting of the Kenya Rift in the Nakuru Area, Based on Geophysical Prospecting

Paolo Conti [1,2,*], Marco Pistis [3,*], Stefano Bernardinetti [1,4,*], Alessio Barbagli [1,4,5,*], Andrea Zirulia [1,*], Lisa Serri [1], Tommaso Colonna [1,4,*], Enrico Guastaldi [1,4] and Giorgio Ghiglieri [3]

1   Center for GeoTechnologies, University of Siena, 52027 San Giovanni Valdarno, Italy; serri@geoexplorersrl.it (L.S.); guastaldi@geoexplorersrl.it (E.G.)
2   Department of Earth, Physical and Environmental Sciences, University of Siena, 53100 Siena, Italy
3   Department of Chemical and Geological Sciences, University of Cagliari, 09100 Cagliari, Italy; ghiglieri@unica.it
4   Geoexplorer Impresa Sociale S.r.l., 52100 Arezzo, Italy
5   Department of Physics and Earth Science, University of Ferrara, 44100 Ferrara, Italy
*   Correspondence: paolo.conti@unisi.it (P.C.); marcopistis75@gmail.com (M.P.); bernardinetti@geoexplorersrl.it (S.B.); barbagli@geoexplorersrl.it (A.B.); zirulia@geoexplorersrl.it (A.Z.); colonna@geoexplorersrl.it (T.C.)

Abstract: In this paper, we present results of tectonic and geophysical investigations in the Kenya Rift valley, in the Nakuru area. We compiled a detailed geological map of the area based on published earlier works, well data and satellite imagery. The map was then integrated with original fieldwork and cross sections were constructed. In key areas, we then performed geophysical survey using Electrical Resistivity Tomography (ERT), Hybrid Source Audio MagnetoTelluric (HSAMT), and single station passive seismic measurements (HVSR). In the study area, a volcano-sedimentary succession of the Neogene-Quaternary age characterized by basalts, trachytes, pyroclastic rocks, and tephra with intercalated lacustrine and fluvial deposits crops out. Faulting linked with rift development is evident and occurs throughout the area crosscutting all rock units. We show a rotation of the extension in this portion of the Kenya rift with the NE–SW extension direction of a Neogene-Middle Pleistocene age, followed by the E–W extension direction of an Upper Pleistocene-Present age. Geophysical investigations allowed to outline main lithostratigraphic units and tectonic features at depth and were also useful to infer main cataclasites and fractured rock bodies, the primary paths for water flow in rocks. These investigations are integrated in a larger EU H2020 Programme aimed to produce a geological and hydrogeological model of the area to develop a sustainable water management system.

Keywords: East African rift system; Kenya; tectonics; geophysics

1. Introduction

The East African Rift System is an active divergent boundary between the Nubian and Somalia plates (Figure 1) and is the ideal place to investigate the mechanisms and dynamics of continental rifting and breakup. Thanks to these ideal conditions a large amount of geological, volcanological and geophysical investigations were carried out over the years and a large amount of data were acquired, especially about relationships between tectonics, magmatism, and sedimentation (see reviews in [1–5]). Tectonic investigations have greatly developed in recent times due to the availability of high resolution satellite imagery, that coupled with structural field investigations in the key areas led to better understanding the role of magmatism to initiate rifting, the role of fluids for wakening of the continental lithosphere and the role of preexisting tectonic features for breakup geometry and faults development [5–11].

In order to better understand the geometry and kinematics of rifting in the central Kenya rift, we carried out geological fieldwork in the Nakuru area (Kenya). To constrain

the geometry of faults and lithostratigraphic units below widespread alluvial deposits, we extensively used geophysical prospecting: (a) electrical resistivity imaging methods, because of their effectiveness to distinguish main subsoil lithologies and locate faults, and (b) the horizontal-to-vertical spectral ratio technique (HVSR), a method widely used in seismic exploration as a cost-effective survey to assess seismic-amplification effects in terms of S-wave resonance frequency, applied to achieve information about the spatial variability of shallow deposits thickness.

Integration of geological and geophysical investigations led to better constrains on the geometry and kinematics of this section of the Kenya rift.
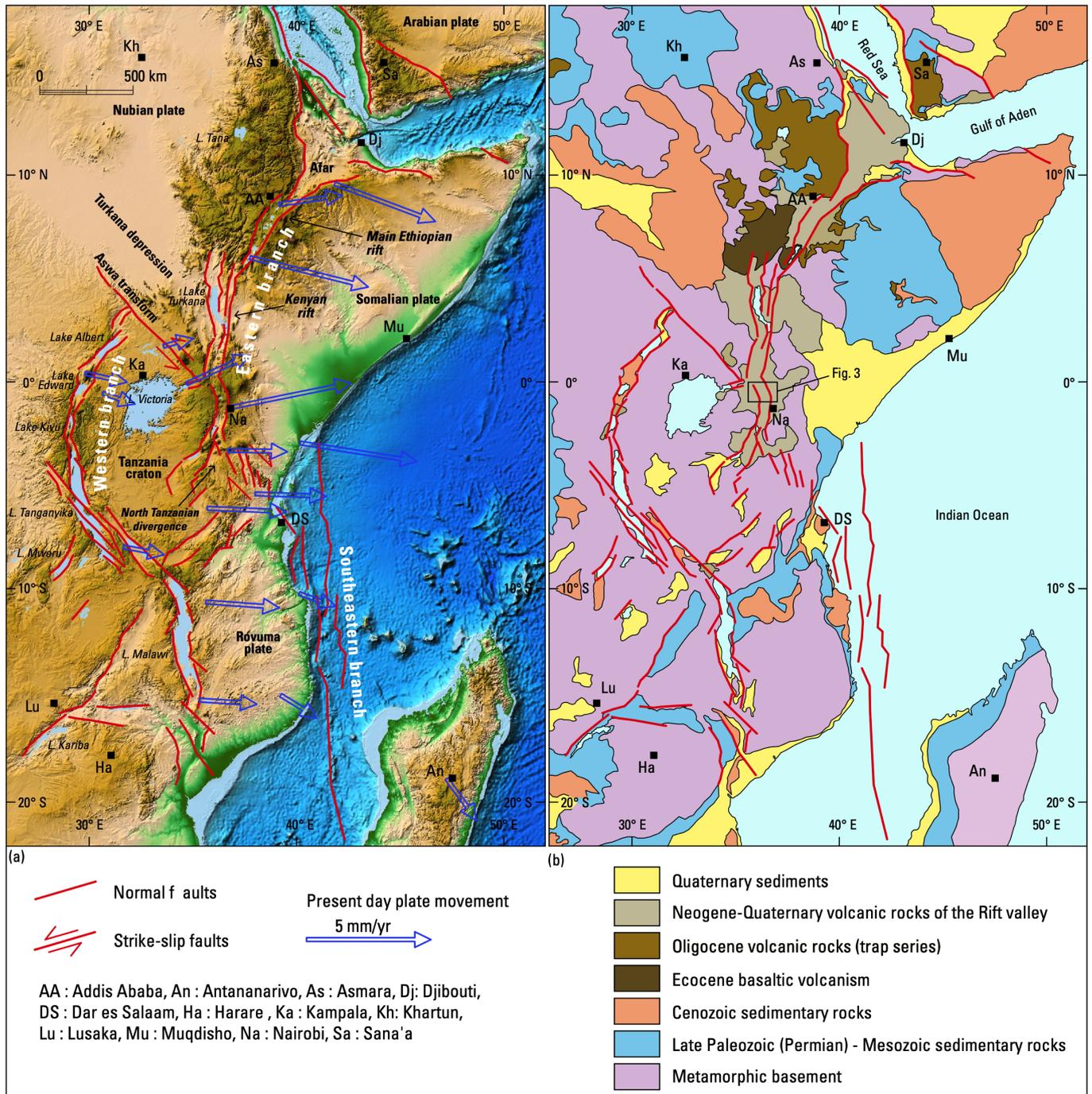

Figure 1. (**a**) Main tectonic features of the East African Rift System, after Chorowicz [1], background image by NOAA [12]. Present day plate movement after Saria et al. [4] (Nubian plate fixed). (**b**) Geological map, after Persits et al. [13], Geological Survey of Ethiopia [14], Geological Survey of Tanzania [15] and Schlüter [16].

2. Geological Setting

The East African Rift System is a series of half grabens (rift valleys) bounded by border faults that can range in length from 10 to up to 200 km and filled with volcanic rocks and sediments. Borders of rifts valleys are usually uplifted areas with mountain belts and plateaus (Figure 1a). The East African Rift System can be divided in two parts, the Eastern branch and the Western branch. A third southeastern branch includes basins offshore of the Africa coast and Madagascar. The Eastern branch runs from the Afar region (NE Ethiopia) through the main Ethiopian rifts, the Turkana lake rift, the Kenya (Gregory) rift, up to the North-Tanzanian divergence (for extensive discussion see [1,17,18] and references therein).

First evidences of Cenozoic magmatism in the area is linked with mantle plume upwelling and started at 45 Ma (see review in [19]) followed by diffuse flood basalts (trap series) that were emplaced at about 30 Ma [20,21]. These basalts overlie a Paleogene-Neogene and a late Paleozoic-Mesozoic sedimentary succession (Figure 1b), unconformably deposited above a metamorphic basement, belonging to the Arabian-Nubian shield (see [22] for review and references). Starting from the Miocene (Figure 2) plateau uplift occurred and extension affected the area, with the development of rift valleys and associated magmatism and sedimentation.

The study area is located in western Kenya (Nakuru County), in the Kenya rift (Figure 1b). This part of the Kenya rift is in an advanced stage of the rifting processes with magmatism and tectonic events currently located only in the inner trough main rift [2,3,5,23].
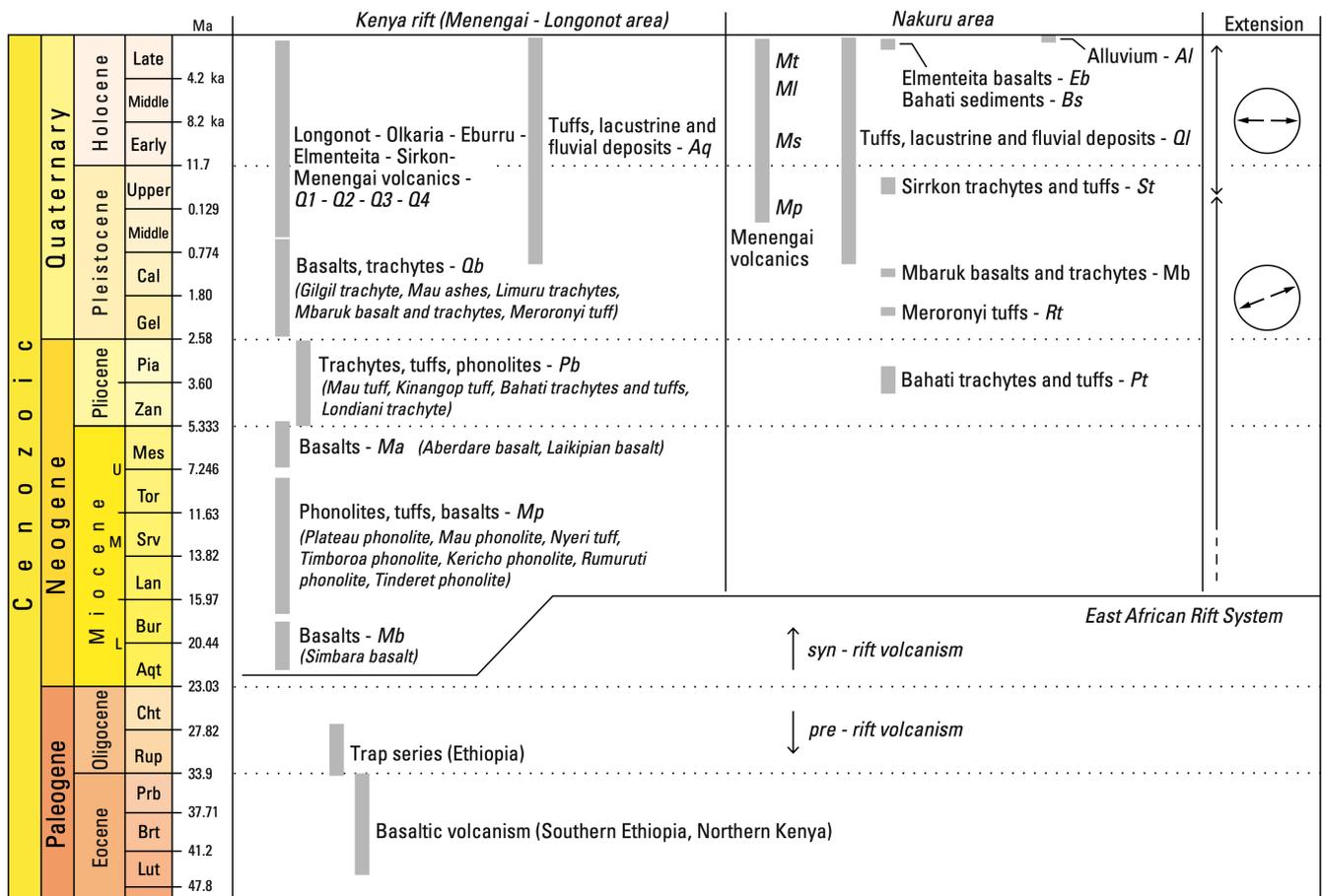
Figure 2. Schematic diagram illustrating volcanic stratigraphy in the Menengai-Longonot portion of the Kenya rift and in the Nakuru area, after Rooney [19], Baker [24], Leat [25], Roessner and Strecker [26]. Labels used in geological map of Figure 3 are indicated, in parentheses are formational names. Age of Oligocene trap series and Eocene basaltic volcanism outside of the study area are reported. Chronostratigraphic scale after Cohen et al. [27]. Extension directions are from this study.

3. The Kenya Rift in the Menengai—Longonot Area

The investigated area is located in the central part of the Kenya rift (Gregory rift). The morphology of the area is the result of its tectonic evolution, and the following main features can be recognized, from W to E (Figures 3a and 4):
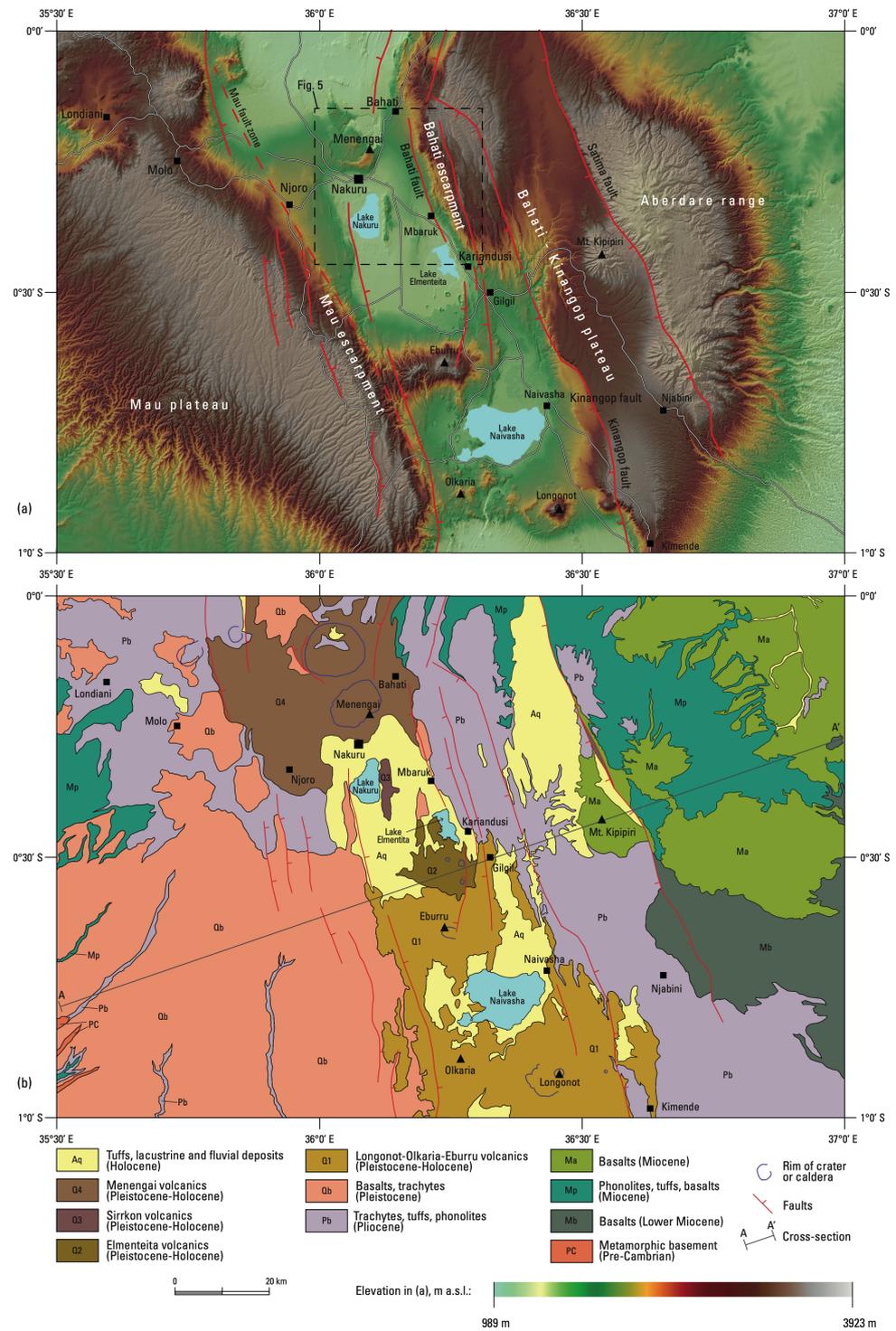

Figure 3. (**a**) Morphology of the Menengai-Longonot and surrounding areas in the central Kenyan rift. (**b**) Geological map of the same area, compiled from maps of Shackleton [28], Thompson and Dodson [29], Thompson [30], McCall [31], Jennings [32], Clarke et al. [33], Williams [34] and original field work. See Figure 1b for location, cross section in Figure 4.
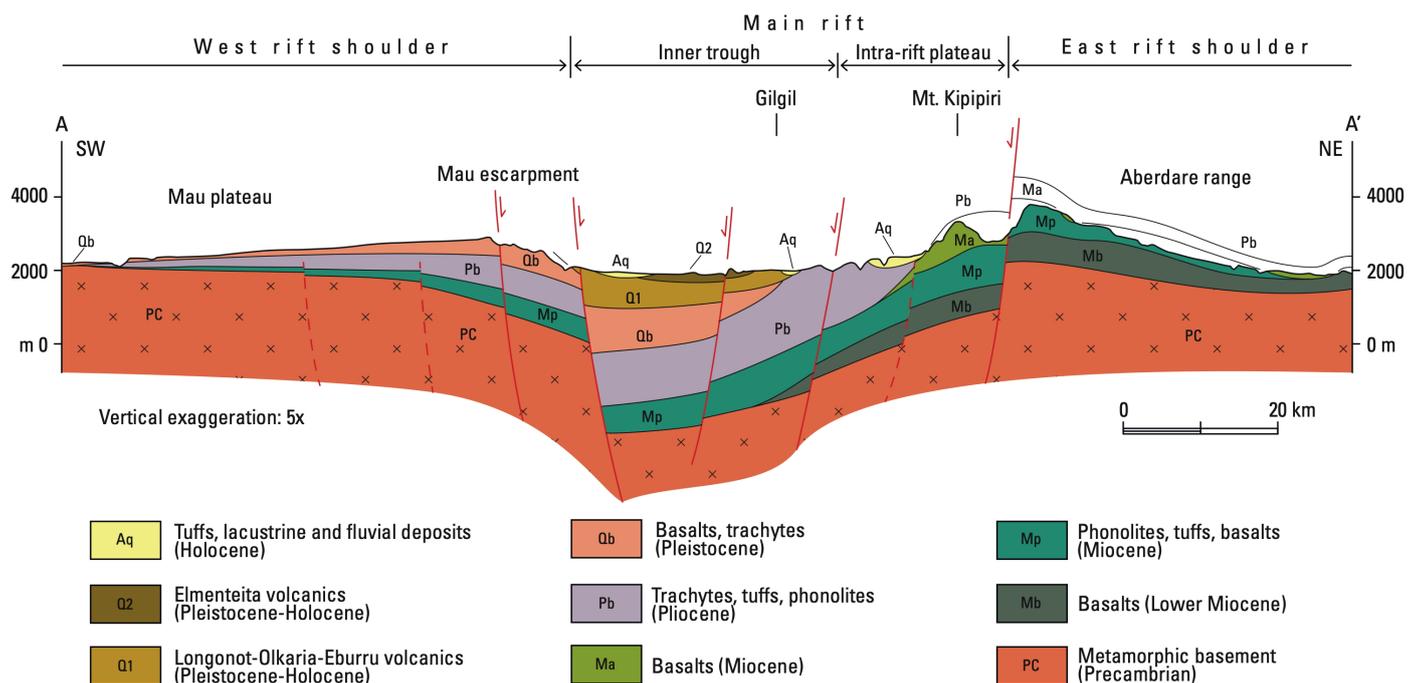
Figure 4. Geological cross-section in the Kenya rift, section trace in Figure 3, based on Baker et al. [35], Smith [36], Roessner and Strecker [26], Simiyu and Keller [37], and original field data.

1. The western rift shoulder (Mau escarpment), bordered by the Mau Fault, a fault system (fault zone) later overprinted by younger faults and partially covered by younger deposits;
2. The inner trough (Lake Nakuru, Lake Naivasha), bordered by the Mau Fault (to the west) and the Bahati and the Kinangop fault (to the east), this is the lowermost portion of the rift valley;
3. The intra-rift plateau (Bahati-Kinangop plateau) bordered by the Bahati and the Kinangop fault (to the west) and the Sattima fault to the east;
4. The eastern rift shoulder (Aberdare range), east of the Sattima fault.

The geological map of the area is presented in Figure 3b. The map is based on original field work, maps of Shackleton [28], Thompson and Dodson [29], Thompson [30], McCall [31], Jennings [32], Clarke et al. [33], Williams [34] and a review of Guth [38].

The oldest rocks in the area are medium- to high-grade metamorphic rocks belonging to the Precambrian basement (labeled PC in Figure 3b), exposed in limited outcrops in the southwestern part of the area. Metamorphic rocks are represented by quartzites, micas-chists, feldspathic and biotite gneisses. Above the basement, a thick Neogene-Quaternary succession of volcanic rocks occurs (Figure 2).

The oldest volcanic rocks in the area are Lower Miocene basalts (Mb in Figure 3b) linked with a sub-aerial fissure and flood style volcanism, during crustal up-warping are most likely related to the presence of a mantle plume [36]. These basalts are present in the eastern part of the area, but are not reported in the western part of the area above the Precambrian basement.

A second large stage of flood volcanism in the same geodynamic context occurred during the Middle-Upper Miocene and is represented by phonolitic lavas with local basalt flows (Mp). This regional flooding event is the largest phase of volcanism in the central Kenya rift and phonolites covered the whole area at this time. In the study area these phonolites are found both in the western and in the eastern rift shoulders.

In the Upper Miocene, volcanism was restricted to the eastern portion of the rift and in the eastern rift shoulder are documented olivine basalts (Aberdare basalts, [35]) with

intercalated trachytic tuffs (Ma). These basalts do not crop out in the western part of the study area.

During the Pliocene the entire area was covered by a thick succession of tuffs, trachytes and phonolites (Pb). It is a important phase of explosive volcanic activity with widespread pyroclastic deposits that extend from the Equator to south of Nairobi. Eruptive sources are not preserved, but facies and thickness analysis suggest they were erupted from the Nakuru-Naivasha area [31,34,35]. A significant thickness of the Pliocene tuffs in the central part of the Kenya rift is therefore expected. This major ignimbritic event can be correlated with an important rifting stage due to penetration of the asthenospheric diapir in the lower crust [36].

Ongoing extension in the central part of the Kenya rift during Lower-Middle Pleistocene led to voluminous volcanism, represented by basalts, trachytes, phonolites, basanites and tuffs (Qb in Figure 3b). These rocks crop out extensively in the Mau plateau and in the main rift, but are missing in the east rift shoulder. This volcanic succession is documented to extend across the Kenya rift south of our study area [35,39].

Younger Quaternary volcanism is limited to the inner trough of the main rift. In the southern part of the area, the Longonot, Olkaria and Eburru volcanic complexes are developed [33], while the Elmenteita and the Sirrkon volcanic complexes are located in the rift center. In the northern part, the main rift is covered by the volcanic rocks of the Menengai volcano. All these volcanic complexes (Q1, Q2, Q3 and Q4 in Figure 3b) are characterized by basaltic and trachytic lava flows, and thick pyroclastic deposits. Contemporaneous with the Quaternary volcanism sedimentation occurred in the area. The sediments (Aq) are represented by conglomerates, sandstones, silts, clays and diatomites of lacustrine and fluvial origin, intercalated with tuffs and volcanic rocks.

For a more detailed description of lithostratigraphic units and tectonics of the Kenya rift and adjoining areas refer to Baker and Wohlenberg [40], Roessner and Strecker [26], Bergner et al. [41], Strecker et al. [42], Williams and Chapman [43], Zielke and Strecker [44], Strecker et al. [42] and references therein.

4. Geology of the Nakuru Area

In this section, we present the stratigraphy and the main tectonic features of the volcano-sedimentary succession in the Nakuru area. The geological map of the area is shown in Figure 5. More tectonic inferences are discussed in the final section after the results of geophysical investigations.

4.1. Stratigraphy

4.1.1. Bahati Trachytes and Tuffs (Pt)

The oldest rocks of the area crop out east of the Nakuru Lake and form the Bahati platform, between the Bahati fault and the easternmost Sattima fault (Figure 3). Limited outcrops are also located SW of Lake Nakuru. They are trachytic ignimbrites with interbedded trachytic lavas and tuffs, with a thickness at least of 250 m [25]. No evidence of volcanic centers related to this succession are documented and it is possible that sources where located west of the Bahati fault, and now covered by more recent deposits.

This succession it is not directly dated, but from relationships with underlying and overlying rocks, a Pliocene age is presumed [25,31].
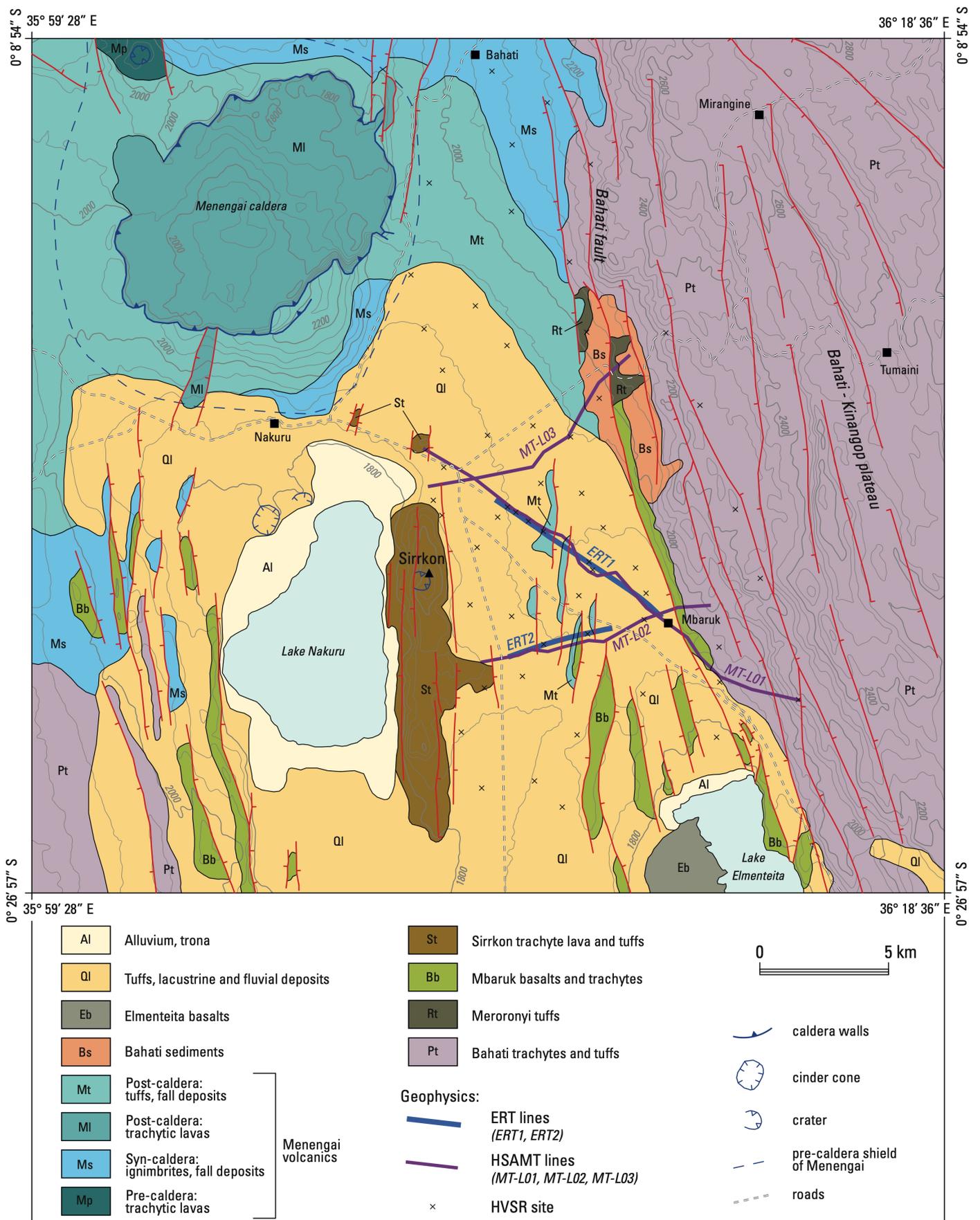
Figure 5. Geological map of the Nakuru area, after Leat [25], McCall [31], Leat [45] and original field work.

4.1.2. Meroronyi Tuffs (Rt)

At about 2 Ma (lower Pleistocene), trachytic lavas were emplaced in this part of the Kenya rift [35]. In the study area, these rocks outcrop near the Bahati fault, above the Bahati Trachytes and Tuffs, and are defined as Meroronyi Tuffs by Leat [25]. The succession is formed by trachytic tuffs, intercalated sediments and welded ignimbrites, with a total thickness of about 30 m.

4.1.3. Mbaruk Basalts and Trachytes (Bb)

The succession is represented by trachytic lavas, followed by thicker basaltic lavas, an upper trachytic lava flow and upper fluviatile sediments, with a total thickness of about 40 m. These are the youngest rocks to crop out all across the rift valley floor and in the study area are exposed in the western part of the Bahati platform (along the Bahati fault), between Lake Nakuru and Lake Elmenteita and also west of Lake Nakuru. West of Lake Nakuru trachytic air-fall tephra are also present (West Lake Trachytes of [25]).

These rocks and deposits are considered to be formed at about 1 Ma. This is supported by K/Ar dating (1.2 Ma [46] and 0.98 Ma in [47]), and correlation with southernmost Gilgil Trachyte [31,33] and Plateau Trachytes (1.3–0.9 Ma, [35]).

4.1.4. Sirrkon Trachyte Lava and Tuffs (St)

East of Lake Nakuru a single volcanic edifice is present, the Sirrkon (or Lion) Hill. This volcanic edifice is cut by N–S striking faults, and now only remnants of a crater are still recognizable. The volcanic succession is represented by trachytic lava flows, pyroclastic and fall deposits. Trachytic lava is also documented north of Sirrkon (Plaat hill and Hyrax hill) and are interpreted by Leat [25] as strombolian cone deposits. The age inferred is late Pleistocene, based on correlation with nearby trachytic rocks outcropping in the area (Menengai volcanics).

4.1.5. Menengai Volcanics (Mp, Ms, Ml, Mt)

The Menengai Caldera is the main topographic feature in northern part of the Nakuru area that developed during the evolution of the Late Quaternary Menengai volcano. The Menengai Caldera is one of the major high-temperature geothermal fields in Kenya and numerous studies have been carried out in the area (see [48–52] for references).

The evolution of the Menengai volcano encompasses three stages:

1. Formation of a shield volcano with low-angle slopes (pre-caldera stage);
2. Collapse of the volcanic edifice and formation of the caldera (syn-caldera stage);
3. Eruption of lavas onto the caldera floor (post-caldera stage).

Pre-Caldera Volcanics (Mp)

Remnants of the shield volcano that developed during the first stage of evolution are still recognizable and form low hills around the Menengai Caldera. The approximate extension of the shield volcano is indicated in Figure 5. This early shield is composed of trachytic lavas and interbedded fall deposits, dated at 0.18 Ma [45] with a maximum thickness of about 300 m. This succession can be observed at the cliffs of the caldera borders or in limited outcrops NW of the Menengai Caldera.

Syn-Caldera Volcanics (Ms)

Between 29,000 and 8500 B.P. [45,53,54], eruption and collapse of the caldera occurred, accompanied by the development of two cycles of trachytic ignimbrites and intercalated air fall deposits, locally separated by sediments. Ignimbrites and air fall deposits cover an area of about 1350 km^2 and can be found up to 30 km from the caldera. Ignimbrites and air fall deposits are found also in the nearby Lake Nakuru and Lake Elmenteita area, interbedded with the ongoing lacustrine sedimentation.

Post-Caldera Volcanics (Ml, Mt)

Post-caldera activity is represented by trachytic lava flows with blocky and ropy morphologies inside the caldera (Ml), as tuffs and air-fall deposits separated by soil horizons outside of the caldera (Mt), and strombolian pumice cones. Two trachytic tuff cones at Honeymoon and Crescent Hill, between Nakuru and Lake Nakuru, are considered satellite vents of the post-caldera series [25].

4.1.6. Bahati Sediments (Bs)

On the Bahati rift shoulders a few meters of sand and silt deposits are locally preserved, derived from erosion of soils and tuffs. Similar deposits are also reported from the Mau plateau, with a thickness of up to 200 m [55].

4.1.7. Elmenteita Basalts (Eb)

In the southern part of the study area (Figure 5) west of Lake Elmenteita, olivine basalts are present [31,33,38]. Basalts are not affected by faulting, so a recent Quaternary age can be inferred. Many cinder cones are present and probably represent the vents from which the basalts were erupted.

4.1.8. Tuffs, Lacustrine and Fluvial Deposits (Ql)

The deposits are represented by conglomerates, sandstones, silts, clays, diatomites and tuffs (tephra) that extensively outcrop around Lake Nakuru and Lake Elmenteita. McCall [31] distinguished the Kariandusi Lake deposits, Kariandusi silts, Lamudiak sediments (Gamblian beds) and Makalia beds, Mboya [56] grouped the deposits in the Kariandusi and Soysambu Formation, Enderit Formation and Ronda Formation. The deposits are of middle Pleistocene-Holocene age (between 15 and 4 ka BP following Bergner et al. [41]).

These deposits represent shallow lacustrine (testified by diatomite occurrence) and fluviatile deposits with intercalation of pyroclastic material. Volcanic activity is documented to be continuous throughout the sequence.

4.1.9. Alluvium, Trona Impregnated Silt (Al)

Recent alluvial deposits occur in swamp area near the Nakuru and Elmenteita lakes. They are usually represented by clay and silt deposits. Silts are often impregnated by trona, a hydrous acid sodium carbonate.

4.2. Tectonics

The study area (Figure 5) shows a flat topography and outcrops with small scale tectonic features exposed are scarce. More considerations can be put forward from analysis of the geological map and the digital elevation model (DEM), presented in Figure 3a.

The main tectonic features of the area are N–S striking normal faults that lowered the central part of the rift. The N–S faults do not cut either the Elmenteita basalts or the Menengai Caldera, of late Holocene age, so their activity before late Holocene can be put inferred. The N–S faults are prevalent in the central part of the area, while more NW–SE striking faults are present in the Bahati-Kinangop plateau. It is important to note that although the main normal faults of the Nakuru area, i.e., the central part of the main rift, are N–S oriented, the main direction of the Kenya rift here is NW–SE, as evident in Figure 3 (strike of the Mau and Bahati escarpment) and in Figure 1.

More discussion about tectonics of the area is presented after presentation of the results of the geophysical investigations.

5. Geophysics

Extensive geophysical fieldwork was performed in the Nakuru area during October and November 2018, aimed to integrate the geological model and observations derived from surface outcrops with deep information. We performed electrical resistivity surveys at two different scales by using Electrical Resistivity Tomography (ERT) and Hybrid Source

Audio MagnetoTelluric (HSAMT). Single station passive seismic measurements (HVSR) were also performed, at 55 locations to achieve information about the spatial variability of superficial deposits thickness across the study area.

The surveys were planned taking into account main geological features and logistical constrains, i.e., the technical suitability of survey areas according to geophysical methods applied. Resistivity measurements (i.e., ERT and HSAMT lines) were located across the Rift Valley east of the Nakuru Lake along three different lines, two orthogonal to the main geological features, here N–S oriented, and one oriented NW–SE crossing the entire valley and reaching the eastern part of the rift. HVSR were spread across all the study area in order to cover as much area as possible. Location of the ERT and HSAMT lines, as HVSR points are shown in Figure 5.

5.1. Electrical Resistivity Tomography (ERT)
5.1.1. Theory and Basic Principles

The purpose of a electrical resistivity survey is to individuate the spatial resistivity distribution in the subsurface. The resistivity ρ of a medium is defined as:

$$\rho = R \cdot \frac{S}{L} \tag{1}$$

where R is the electrical resistance, L is the length of a cylinder and S is the area of its cross section. Conductivity is the inverse of resistivity. The electrical resistance R is defined by Ohm's law as:

$$R = \frac{V}{I} \tag{2}$$

where V is the potential and I is the current. In a homogeneous half-space, with point source of current, the current flow is radial from this point and the electrical equipotential surfaces are hemispherical. In this configuration the potential can be expressed through the resistivity and the current:

$$V = \frac{\rho I}{2\pi R} \tag{3}$$

In an elementary quadripolar configuration, on homogeneous subsoil and with four electrodes called C_1, C_2, P_1, P_2 (Figure 6), the feeding of current from C_1-C_2 dipole, produces current flow and a correspondent potential field with equipotential surfaces, which can be measured through P_1-P_2 dipole. The potential difference measurement between P_1-P_2 dipole can be expressed in analytical way by the equation:

$$\Delta V = \frac{\rho I}{2\pi} \left[\left(\frac{1}{C_1 P_1} - \frac{1}{C_2 P_1} \right) - \left(\frac{1}{C_1 P_2} - \frac{1}{C_2 P_2} \right) \right] \tag{4}$$

where $C_1 P_1$, $C_2 P_1$, $C_1 P_2$ and $C_2 P_2$ represent distances among every couple of electrodes C_1, C_2, P_1, P_2. The electrical resistivity ρ can then be calculated as follows:

$$\rho = K \frac{\Delta V}{I} \tag{5}$$

where:

$$k = \frac{2\pi}{\left(\frac{1}{C_1 P_1} - \frac{1}{C_2 P_1} \right) - \left(\frac{1}{C_1 P_2} - \frac{1}{C_2 P_2} \right)} \tag{6}$$

a geometrical factor that depends on the relative disposition of the four electrodes.
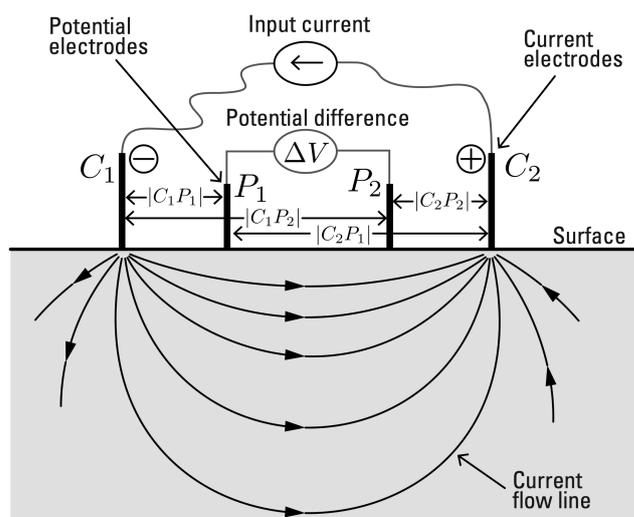
Figure 6. Elementary quadripolar configuration in homogeneous half-space. The current is injected into the subsurface through electrodes (C_1, C_2) installed into the ground, and the resistivity distribution along a profile is measured (electrodes P_1, P_2). Arrows are flow lines of transmitted current.

In non-homogeneous subsoil, the current flow distribution depends on the resistivity of the medium, and it is concentrated into the more conductive volume [57].

The electrical resistivity of rocks and soils is a function of solid part (grain size and mineralogy), pore size distribution and connectivity, fluids content on pore and their resistivity properties and temperature, gas content [57–60].

Electrical resistivity for rocks and soils, range from few $\Omega \cdot m$ to several tens thousands $\Omega \cdot m$ (Figure 7). Most rocks near the Earth's surface are composed by insulating grain minerals and have low conductivity, conduction of electricity is mostly through groundwater contained in the pores of the rocks and along surface layers at the contact of rocks and solution. Soils can have clayey conductive minerals and, rarely, metallic conductive minerals. In the case of clayey soils, resistivity depends on electrical charge density at the surface and is related to the cations exchange capacity. When massive metallic minerals are present without discontinuities the current flow is due to the free electron displacement.
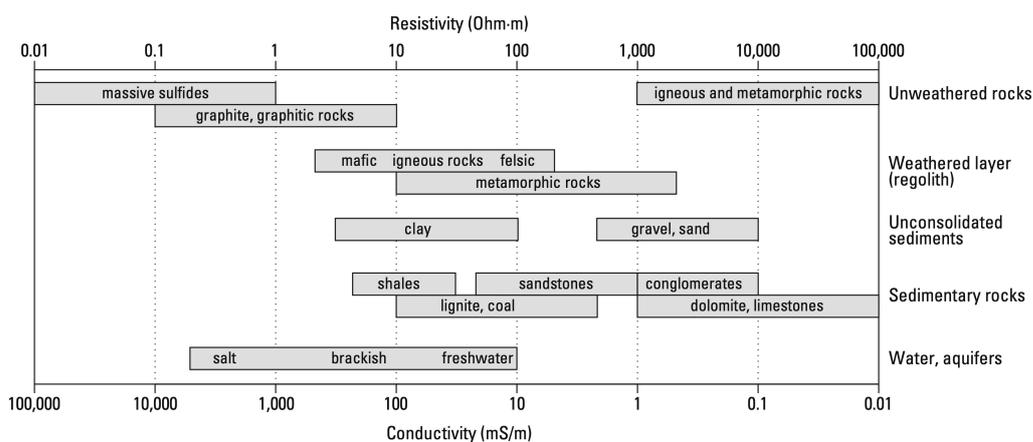

Figure 7. Resistivity values of various rock types and materials, from Palacky [61].

5.1.2. Data Acquisition

We distributed two ERT lines across the study area (Figure 5), the two profiles have a length of 7670 m and 3830 m, for profile ERT1 and ERT2, respectively. The high-resolution geoelectrical resistivity measurements were performed using the georesistivimeter Syscal-Pro Switch from IRIS Instruments. In order to reach a maximum depth and extend laterally

along the profile, the roll-along technique was applied and the measurements were performed using the georesistivimeter Syscal-Pro Switch from IRIS Instruments. The base configuration adopted was with 96 electrodes (10 m spaced) and the array was moved forward each time with an overlap of 48 electrodes (half of a single profile). In order to explore the subsurface and highlight the lithological variations both in vertical and horizontal direction, we preliminary tested over a portion of the profile ERT1 four quadripolar configurations: Dipole–Dipole (DD) and Schlumberger Reciprocal (SR) optimized for multichannel measurements, Wenner (W) and Wenner–Schlumberger (WS) for single channel measurements [62]. The Schlumberger reciprocal is a manipulation of the classical Schlumberger with the current electrodes in the inner part of the quadripole.

As Figure 8 shows, the DD configuration produces the poorest signal among the applied configurations, where the 65% of the measures have a ΔV lower than 1 mV. As expected, W and WS have the strongest signals with a mode equal to 10 mV. The higher frequencies of $V_p > 10$ mV, obtained by the W configuration compared to the WS configuration are probably due to the lower n factor. In terms of root-mean squared error (RMS) between observed and calculated apparent resistivity we detect the best result for the Wenner–Schlumberger and the worst for the Dipole–Dipole configuration (Table 1).
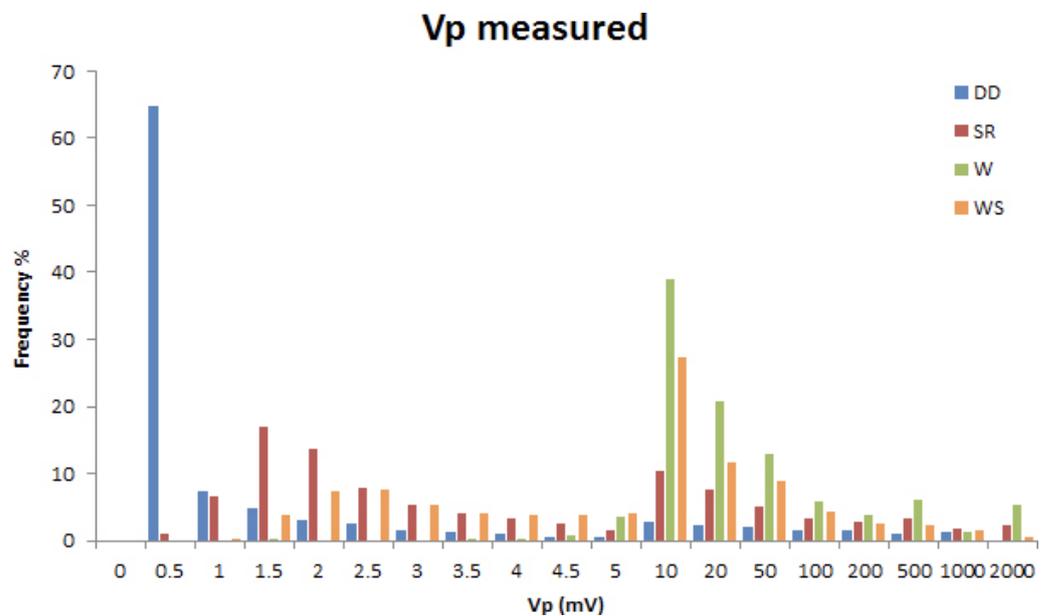

Figure 8. Frequency distribution of measured voltage for each of the tested configuration. Dipole–Dipole (DD), Schlumberger Reciprocal (SR), Wenner (W) and Wenner–Schlumberger (WS).

Table 1. Root-mean squared error (RMS) values of the inversion of data acquired with the four different quadripolar configuration.

	Dipole Dipole	Schlumberger Reciprocal	Wenner– Schlumberger	Wenner
RMS at 4 iteration	37.9	13.5	4.1	7.1

Based on all the above considerations, the Wenner–Schlumberger was chosen as most suitable configuration to perform the ETR survey.

5.1.3. Data Processing

In order to process the electrical resistivity data, we applied RES2DINV V. 4.03.13 [63] inversion routine. The data processing can be described in two main steps. In the

first step bad data were removed by using both threshold values on each measurement (st-dev > 5%, abs (ΔV) < 1 mV, apparent resistivity $< 0\ \Omega \cdot$m) and identification of the outliers. In the second step, we carried out the tomographic inversion starting from apparent resistivity values. The robust constraint (L1-norm) on inversion method [62] was applied for the processing of the resistivity model, since the algorithm attempt to minimize the absolute changes in the resistivity values and, therefore, to produce models with sharp interfaces between different regions with a high contrast of resistivity.

The optimization method used by the inversion routine of RES2DINV basically tries to reduce the difference between the calculated and measured apparent resistivity values by changing the resistivity of the model blocks. This difference can be assessed by the RMS. The routine stops when a defined number of iterations is reached or the variation in terms of RMS is lower than a threshold value and successive iterations do not improve the results. However, the model with the lowest possible RMS error can sometimes show large and unrealistic variations in the modelled resistivity and might not always be the "best" model from a geological perspective. In general, the most prudent approach is to choose the model at the iteration after which the RMS error does not change significantly. This usually occurs between the 3rd and 5th iterations [63].

Finally, RMS values were used to remove noisy data, where the percentage difference between the observed and calculated apparent resistivity was far and well separated from the average values.

5.2. Hybrid Source Audio Magnetotellurics (HSAMT)

5.2.1. Theory and Basic Principles

The magnetotelluric method or magnetotellurics (MT) is a passive exploration technique to infer the electrical properties of the Earth's subsurface [64–66]. Interaction of the solar wind with the magnetosphere and worldwide thunderstorm activity produce variations of the Earth Magnetic Field, inducing electric currents (telluric currents) in the Earth's subsurface. These telluric currents are the energy source used by magnetotellurics. Measurements of naturally occurring variations of the magnetic field at the Earth's surface (B_t) and the induced electric field (E_t) provide information about subsurface electrical resistivity and therefore about rocks and geological structures in the Earth's interior. The main advantage of this method is its capability for exploration from shallow to very great depths (from a few tens of meters to several hundreds of kilometers), without the use of an artificial power source. For more information about the method refer to Campbell [67], Simpson and Bahr [68], Chave and Jones [69], and references therein. In the case of HSAMT, a combination of natural MT signals and human-made (hybrid sources) signals are measured, to overcome the problem of weak-amplitude of the signal in the frequency range from 0.8 to 64 kHz.

5.2.2. Data Acquisition

During this study, we used the Stratagem EH4 Conductivity Imaging System (by Geometrics, Inc. and Electromagnetic Instruments Inc., ver. 2.19) to perform the HSAMT survey. The Stratagem EH4 system consists of two basic components: a receiver and a standard transmitter. The latter is used to provide additional high-frequency signals in the range from 0.8 to 64 kHz, where natural signals are weak and, therefore, improve data quality. Electric dipoles and magnetometers are laid out in perpendicular directions (i.e., E_x, E_y, B_x and B_y) and both natural and transmitted frequencies are recorded from distant and non-polarized sources.

In this study, we carried out a total of 35 soundings along three profiles (Figure 5) within the frequency range from 10 Hz to 100 kHz. The dipole length was fixed at 25 m, and the coils followed the right-hand rule, with the z axis directed to increasing depth. The antenna was located at an average distance of 250 m from the acquisition station, far enough to avoid near-field effects due to the low resistivity subsurface values at the site. For each sounding an oversaturated NaCl solution was used to improve the ground

coupling with the electrodes. Along the MT_L1 line, we carried out 18 soundings with X azimuthal direction N120°; along the MT_L2 line, we carried out nine soundings with X azimuthal direction N250°; and along the MT_L3 line, we carried out eight soundings with azimuthal direction N2100°.

5.2.3. Data Processing

After the data recording by Stratagem EH4, data geometry was first corrected according to the coordinates obtained on the site by GPS measurements. After the geometry correction, the first step of the data processing is the mesh building. The mesh was discretized in the x-direction using a regular spacing and in the z-direction using an incremental spacing from one layer to another, with a factor of 1.1. The maximum depth of the grid was chosen according to an average depth obtained by the one-dimensional inversions, and correspond to 700 m, as an initial resistivity value of 10 Ωm was assigned to the whole mesh.

Aiming to obtain the most correct data performance and reduce the data noise level, two smoothing operations were applied on the data: one on the transversal magnetic (TM) mode and one on the transversal electric (TE) mode. In order to remove possible distortion of resistivity images due to superficial inhomogeneity of the geological structures present in the investigated subsoil, the static shift correction was applied to the TM mode (the TE mode is not considerably affected by this error).

The inversion was then computed using the effective impedance and the "smoothness constrain". The "smoothness constrain" uses a procedure based on the Gauss-Newton least-squares method and returns a stable parameter distribution. The resistivity limits of the model were set at 1–5000 Ωm and the inversions where terminated after a fixed number of iterations (i.e., 34). The first four inversions were used to correct the galvanic effects due to the connections between the electrodes and the earth. The remaining 30 inversions were sufficient to obtain a satisfactory image with a low RMS.

5.3. Horizontal to Vertical Spectral Ratio (HVSR)

5.3.1. Theory and Basic Principles

The horizontal-to-vertical spectral ratio (HVSR or H/V) technique is used to retrieve information about the shallow-subsoil seismic properties by single-station measurements performed on the soil surface [70–73]. This method, widely used as a cost-effective survey to assess seismic amplification effects, is therefore useful to evaluate the presence of impedance contrast, its magnitude and estimate the thickness of cover deposits.

The HVSR is a curve that represents the value of the ratio between the average spectral amplitudes of the environmental vibrations as a function of frequency. This is an experimental evaluation of the spectral amplitude ratios between the horizontal components (N–S, E–W) and the vertical component of the environmental vibrations on the ground surface measured at a point with a special three-axial seismometer [70,74].

In the field of environmental vibrations, there are both volume waves (P and S) and surface waves (Love and Rayleigh) and their contribution to the total produced energy varies from case to case and depends on the frequency range considered. Seismic noise can be linked both to a natural origin (low frequencies) or to human activity (high frequency) [72].

The fundamental assumption of the microtremor analysis is that the multiple reflections of the seismic waves, which remain trapped in the sedimentary cover lying on the stiffer material, give rise to constructive interferences that are the cause of resonance. The frequency of the peaks identified in the HVSR curves presents a non-linear and inversely proportional relationship with the thickness of soft shallow layers. This relationship is expressed by Equation (7) where f is the fundamental resonance frequency, V_s is the average velocity of S waves of the layer and H is the thickness of the soft layer [75,76].

$$f = \frac{V_s}{4H} \tag{7}$$

Equation (7) shows that H/V survey can also provide indications of stratigraphic nature: starting from a measure of environmental vibrations that limit the frequency value and the shear velocity of the coverage, the depth of the main seismic reflectors can be estimated or vice versa.

5.3.2. Data Acquisition

The digital tromograph TROMINO Engineering by Micromed, with nine channels and a built-in GPS receiver was used to perform the HVSR survey. The choice of location of the acquisition points was identified in the areas far from anthropic or natural structures (fences, buildings, roads, trees) that could interfere with the survey. Four preliminary measurements of 20 min were performed to evaluate the signal quality. Following the results of the preliminary measurements, the recording length was extended to 30 min in order to compensate for the presence of noisy transient events. The sampling frequency was set at 128 Hz for all the measurements. For a common evaluation of the signal directionality, the instrument was oriented to the magnetic north. Before data recording, the area around the Tromino was cleaned up of the elements that could generate transient events such as grass and stones.

5.3.3. Data Processing

The analysis of entire passive seismic survey was performed through the software Grilla ver. 7.5 (MoHo s.r.l. release 2018) which accompanies TROMINO. In Grilla, the three components of the seismic signal are represented in terms of spectral powers (square of the acceleration normalized to the frequency) from which the ratio trend between the horizontal spectral components and the vertical component is extrapolated as a function of frequency.

The recordings were divided into time intervals (i.e., windows) of 20 s and then a spectral analysis of the three components was performed and the spectral ratio for each of the windows obtained was calculated. All the HVSR data have been obtained by smoothing the spectra with a triangular smoothing function with a width equal to 10% of the central frequency. The final H/V curve was obtained as the average of the spectral ratios on all segments. In addition, for each data was generated a directional graphic which helped on the evaluation of the observed peak and a temporal stationary graph of the H/V spectral ratio.

For each observed peak, its validity was assessed by the SESAME criteria [77]. These criteria allow to evaluate the quality of the signal processing and the significance of the H/V peaks from a statistical point of view. In case the of failure to pass the SESAME criteria, it does not mean that there are no significant resonances but only that there are no well-defined individual peaks.

Finally, the frequency peaks individuated by HVSR were interpolated with the aim to produce a frequency map representative of the spatial variability of the impedance contrast detected (Figure 9).
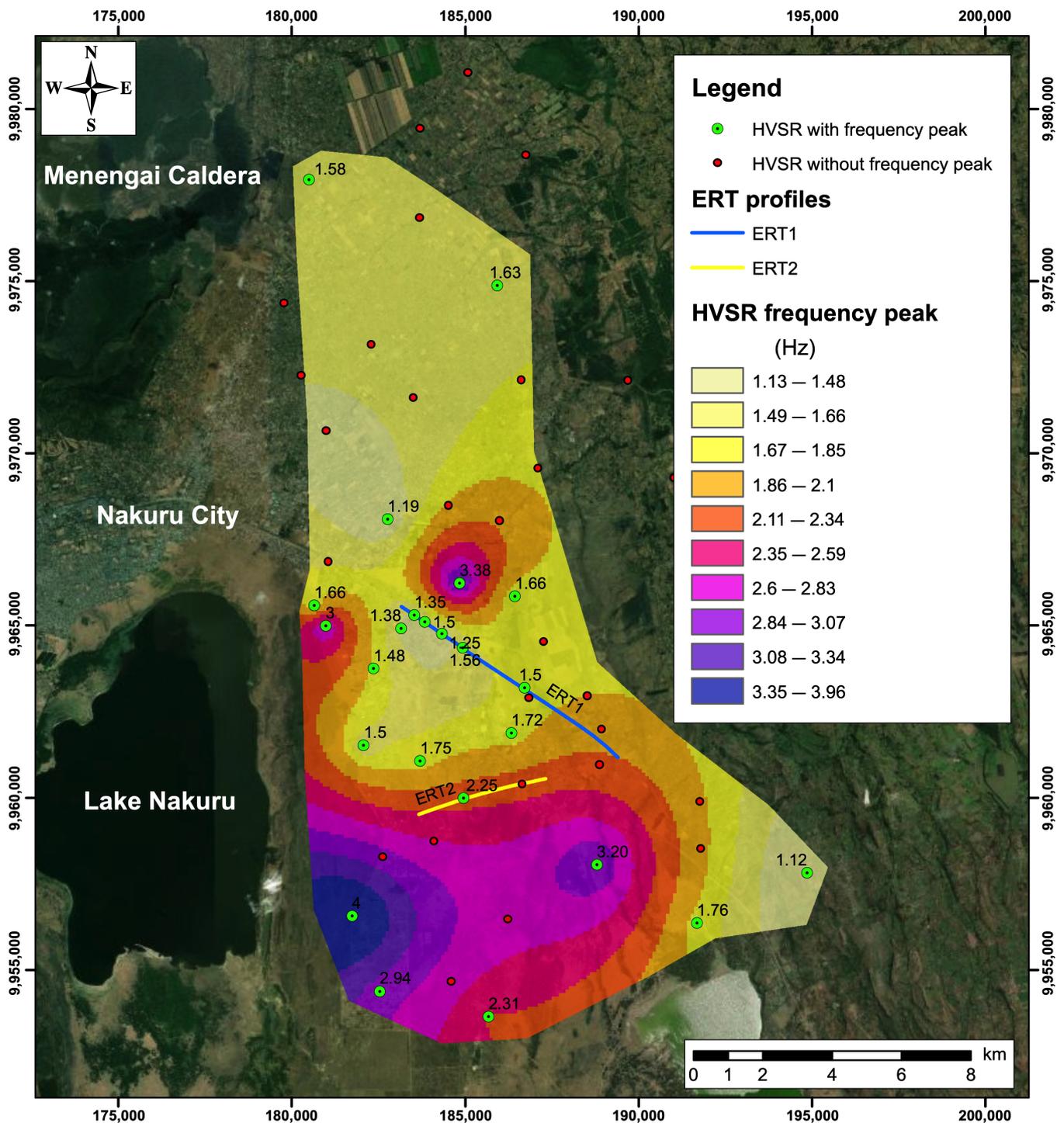
Figure 9. Frequency map for the study area, based on HVSR data. ERT lines are indicated.

6. Results and Discussion

Most rocks near the Earth's surface have high resistivity (Figure 7). Conduction of electricity negligibly occurs through the silicate crystalline lattice, but mostly through movement of ions in groundwater (solution) contained in the interconnected pore spaces, along the interface between pore space and pore walls, along grain boundaries and along fractures. Since the ions which conduct current are responsible for conductivity/resistivity of rocks, solutions with large number of ions (e.g., rocks with saline water in pores) will have the higher conductivity (lower resistivity). In general, the main factors that influence

resistivity in rocks are porosity, temperature, rock texture, rock type, presence of clay minerals, water saturation, salinity of water and fluid permeability, as indicated in Table 2.

Geophysical explorations carried out so far in the study area were mainly oriented to investigate the geothermal potential in this portion of the Kenya Rift valley [50,78,79]. Sosi [80] and Sosi et al. [81] performed combined studies based on vertical electrical soundings and pumping tests, for groundwater flow assessment at the Kabatini well field (northern portion of our study area), highlighting layered models with large resistivity variations.

Figure 10 shows two geological cross section across the Nakuru area that we constructed on the background geology of Figure 5, with resistivity values from our geophysical surveys. The following resistivity values were recorded:

1. Quaternary tuffs, lacustrine and fluvial deposits (Ql) show resistivity of about 50–200 Ωm, the most superficial portion of these deposits (first few meters of soil deposits) shows lower resistivity (30–50 Ωm);

2. Menengai post-caldera tuff and fall deposits (Mt) show lowest resistivity (5–20 Ωm), syn-caldera ignimbrites and fall deposits (Ms) show slightly higher resistivity values (20–50 Ωm);

3. Mbaruk basalts and trachytes, Meroronyi tuffs and Bahati trachytes and tuffs (Bt) are grouped together and show resistivity values of about 50–100 Ωm;

4. The high values of resistivity observed in the western portion of section ERT2 (Figure 10a) is assumed to be related to occurrence of predominantly lava flows, probably of the Sirrkon trachyte lava and tuffs (St) (500–1000 Ωm).
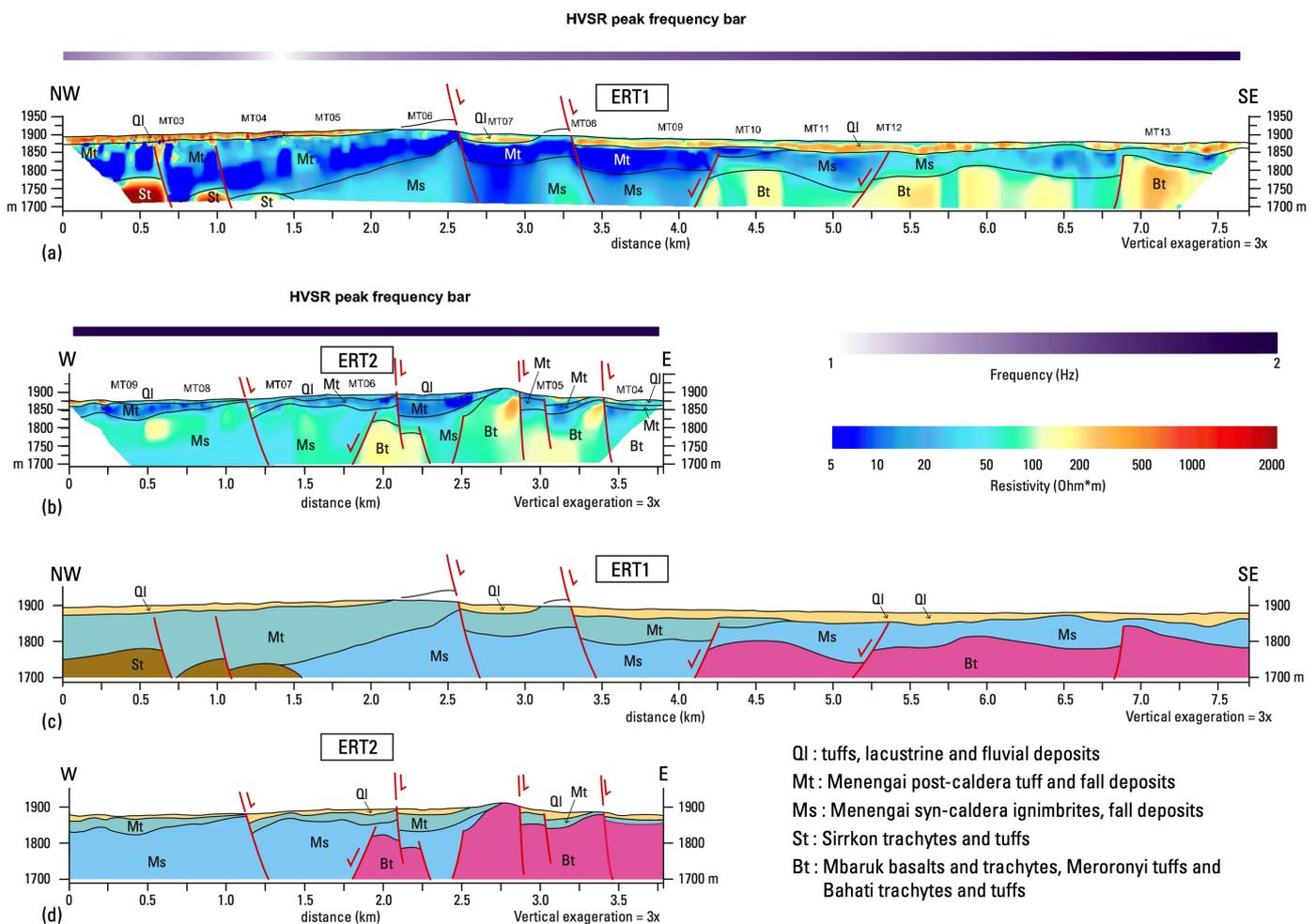

Figure 10. Cross sections with resistivity data, see Figure 5 for location. (**a,b**) ERT1 and ERT2 lines based on electrical resistivity tomography (ERT) data. (**c,d**), Geological cross-sections.

From both sections, we can infer that the very first meters of soils have low resistivity, probably linked with soil moisture and water content. The underlying tuffs, lacustrine and fluvial deposits (Ql in Figure 10) show higher resistivity due to induration and carbonate precipitation. Pyroclastic deposits and pyroclastic rocks show resistivity values far below the typical values for igneous rocks (see Figure 7), this can be related to their high porosity. Underlying basalts and trachytes (St and Bt in Figure 10) have higher resistivity than the pyroclastic deposits.

Figure 11 presents three cross-sections based on HSAMT that reach a deeper depth, and incorporate Figure 10 sections. Due to the smaller scale, the Quaternary tuff, lacustrine and fluvial deposits, the Menengai volcanics and the Bahati sediments are rendered all together and labeled "At". In these sections, the resistivity variations are larger than in Figure 10, ranging from a few Ωm to values of about 3000 Ωm. In the upper portion of the MT-L01 section lower resistivity rocks and deposits are present (mainly unconsolidated pyroclastic rocks, labeled as "At"), that overlay rocks with higher resistivity represented by predominantly trachytes and basalts (St and Bt). In the central and eastern part of the section significant lower resistivity values are recorded, that we interpret are related to presence of cataclastic and fractured rocks with the increased porosity and water content. Significant contribution to lowered resistivity of rocks in this area can be also linked to alteration of volcanic rocks along a fault zone, with production of alteration minerals as smectite and zeolites that usually have high cation exchange capacity and therefore high conductivity [82], as pointed out in the Menengai geothermal area [83].
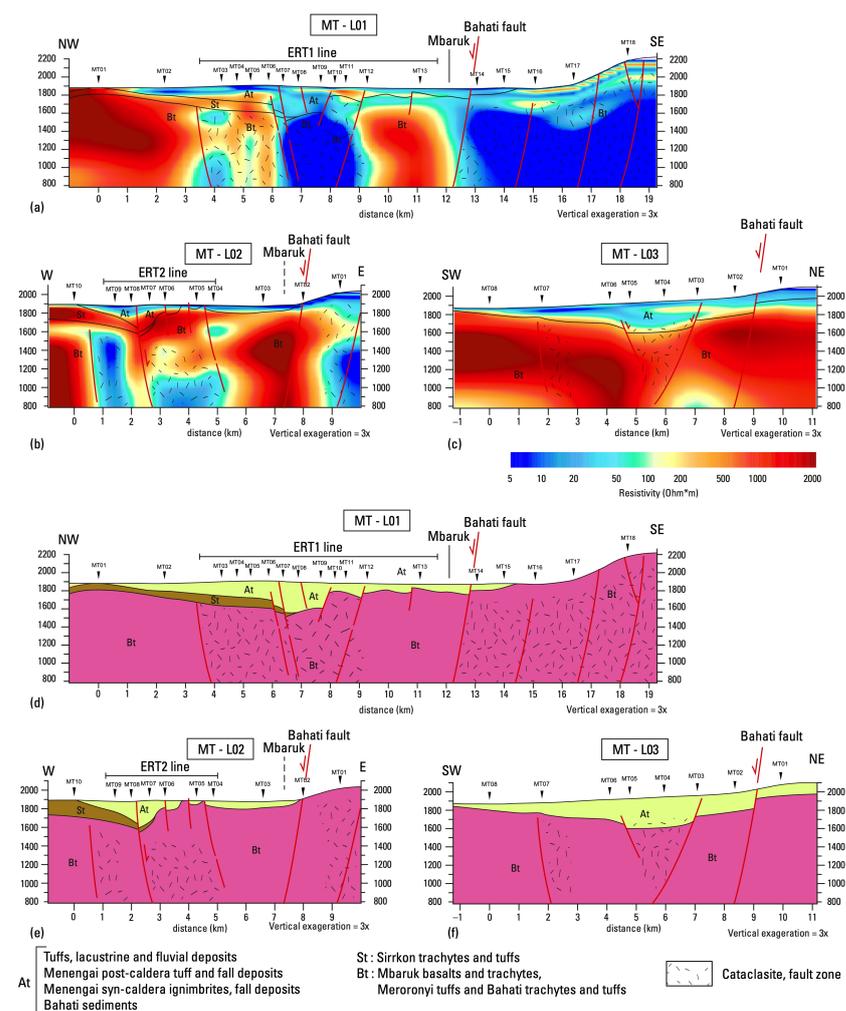

Figure 11. (**a**–**c**) Cross section based on magnetotelluric (HSAMT) and HVSR data. (**d**–**f**) Geological cross-section. See Figure 5 for location. Sections include data from ERT1 and ERT2 lines (Figure 10).

Table 2. Effect of geological processes on resistivity, after Ward [84]. Effect of rock type is illustrated in Figure 7.

Geological Process	Resistivity
Porosity	decrease
Temperature	decrease
Well sorted sandstones with voids	decrease
Poorly sorted sandstones	increase
Sandstones with matrix/cement	increase
Magmatic texture (low porosity)	decrease
Fracturing/faulting	decrease
Water saturation in pores	decrease
Water salinity	decrease
Shale/clay content	decrease
Clay alteration	decrease
Weathering	decrease
Induration	increase
Carbonate precipitation	increase
Silicification	increase

The Bahati fault is the main tectonic feature in the surveyed area (Figures 10 and 11), a west-dipping normal fault that led to uplift of the footwall Pliocene trachytes, tuffs and phonolites of the Bahati-Kinangop plateau. This fault is evident in profiles MT-L01 and MT-L02 of Figure 11 with low resistivity rocks in its footwall, probably due to widespread fracturing. This is not evident in the northern profile MT-L03, where high resistivity rocks are present throughout at depth. The Bahati fault has a strong geomorphological expression in the Mbaruk area, but is less evident to the the north in the Bahati and Kariandusi-Gilgil-Eburru areas (Figure 3), where it is overprinted by N–S striking faults. Consequently, we can infer that NW–SE striking normal faults are overprinted by N–S normal faults. This is also evident from Figure 3, where the NW–SE striking Mau Fault, responsible for the uplift of the Mau escarpment at the footwall, is not overprinted by N–S striking faults south of Njoro. Therefore, we argue that a change in extension direction occured in this part of the Kenya rift, from a NE–SW extension to E–W extension, as also documented at a larger regional scale [42,85,86]. Age constrains for this deformation can be inferred from geological map of Figure 5, where it is evident that the volcanic succession of the central part of the map (Sirrkon trachytes and tuffs and younger deposits) are affected by N–S striking faults only. Based on this evidence, we can argue that E–W extension predominated starting from the upper Pleistocene, i.e., after the emplacement of the Sirrkon trachytes and tuffs. NE–SW extension prevailed during the Miocene-Upper Pleistocene time span and it was responsible of the present-day large-scale NE–SW orientation of the Kenya rift. Time intervals of extension phases are also shown in Figure 2.

7. Conclusions and Final Remarks

Our investigations in the central part of the Kenya rift in the Nakuru area, Kenya (Gregory rift) included geological field work, together with geophysical prospecting. A careful analysis of geological maps available and original field work led first to compilation of a regional geological map (Figure 3) and a detailed geological map for the Nakuru area (Figure 5). To unveil the main tectonic features of the area and their prolongation at depth, geophysical investigations were carried out in the central part of the main rift zone, west of the Lake Nakuru. We studied electrical resistivity of rocks in the area first with Electrical Resistivity Tomography (ERT) methods and then with Audio MagnetoTelluric (HSAMT) methods. All these data were integrated with single station passive seismic measurements (HSVR).

All information was used to construct geological cross-sections that illustrate the shallow tectonic structure of the Kenya rift in this area (Figures 10 and 11). The central part of the main rift is characterised by a close spaced system of normal faults, striking N–S, well developed in the inner trough of the Rift valley, W and especially E of Lake Nakuru.

These normal faults crosscut almost all the volcanic succession of the area and a Holocene age for their activity can be inferred. Therefore, the most recent extension direction in this portion of the Kenya rift is E–W. Magnetotelluric and HVSR data allow us to trace the main tectonic features at depth and to construct geological cross-sections from the Bahati plateau to Nakuru Lake (Figure 11). In these sections, the relevant thickness of the upper Pleistocene-Holocene pyroclastic rocks (and less developed trachytes and basalts) is shown. Faults can be traced at depth and cataclastic and fractured zones developed along the faults, as it can be observed from lateral variation of rock resistivity gathered from geophysical investigations.

At a smaller scale (Figure 3), the main faults affecting the Bahati-Kinangop plateau, the Mau plateau and developing the Bahati and Mau escarpment are NW–SE oriented. This is also the orientation of the Kenya rift at a larger regional scale. These faults affected the Miocene-middle Pleistocene succession and are absent from the Holocene volcano-sedimentary succession of the inner trough in the main rift. Therefore, we can infer for these NW–SE oriented faults Miocene-middle Pleistocene activity with the main extension direction oriented NE–SW. Our investigations point out to a change in the extension direction in the Gregory rift, from NE–SW to E–W, that occurred in the upper Pleistocene.

References

1. Chorowicz, J. The East African rift system. *J. Afr. Earth Sci.* **2005**, *43*, 379–410. [CrossRef]
2. Ebinger, C. Continental break-up: The East African perspective. *Astron. Geophys.* **2005**, *46*, 2.16–2.21. [CrossRef]
3. Corti, G. Continental rift evolution: From rift initiation to incipient break-up in the Main Ethiopian Rift, East Africa. *Earth-Sci. Rev.* **2009**, *96*, 1–53. [CrossRef]
4. Saria, E.; Calais, E.; Stamps, D.; Delvaux, D.; Hartnady, C. Present-day kinematics of the East African Rift. *J. Geophys. Res. Solid Earth* **2014**, *119*, 3584–3600. [CrossRef]
5. Muirhead, J.; Kattenhorn, S.; Lee, H.; Mana, S.; Turrin, B.; Fischer, T.; Kianji, G.; Dindi, E.; Stamps, D. Evolution of upper crustal faulting assisted by magmatic volatile release during early-stage continental rift development in the East African Rift. *Geosphere* **2016**, *12*, 1670–1700. [CrossRef]
6. Corti, G. Control of rift obliquity on the evolution and segmentation of the main Ethiopian rift. *Nat. Geosci.* **2008**, *1*, 258–262. [CrossRef]
7. Beutel, E.; van Wijk, J.; Ebinger, C.; Keir, D.; Agostini, A. Formation and stability of magmatic segments in the Main Ethiopian and Afar rifts. *Earth Planet. Sci. Lett.* **2010**, *293*, 225–235. [CrossRef]
8. Hui, H.; Peslier, A.H.; Rudnick, R.L.; Simonetti, A.; Neal, C.R. Plume-cratonic lithosphere interaction recorded by water and other trace elements in peridotite xenoliths from the Labait volcano, Tanzania. *Geochem. Geophys. Geosyst.* **2015**, *16*, 1687–1710. [CrossRef]
9. Katumwehe, A.B.; Abdelsalam, M.G.; Atekwana, E.A. The role of pre-existing Precambrian structures in rift evolution: The Albertine and Rhino grabens, Uganda. *Tectonophysics* **2015**, *646*, 117–129. [CrossRef]
10. Mana, S.; Furman, T.; Turrin, B.D.; Feigenson, M.D.; Swisher, C.C., III. Magmatic activity across the East African North Tanzanian divergence zone. *J. Geol. Soc.* **2015**, *172*, 368–389. [CrossRef]
11. Muirhead, J.; Kattenhorn, S. Activation of preexisting transverse structures in an evolving magmatic rift in East Africa. *J. Struct. Geol.* **2018**, *106*, 1–18. [CrossRef]

12. National Oceanic and Atmospheric Administration. ETOPO1 Global Relief Model—National Oceanic and Atmospheric Administration. 2019. Available online: https://ngdc.noaa.gov/mgg/global/relief/ETOPO1/image/ (accessed on 9 February 2021).

13. Persits, F.; Ahlbrandt, T.; Tuttle, M.; Charpentier, R.; Brownfield, M.; Takahashi, K. *Map Showing Geology, Oil and Gas Fields and Geologic Provinces of Africa*; Open-File Report 97–470 A; U.S. Geological Survey: Sioux Falls, SD, USA, 2002.

14. Geological Survey of Ethiopia. *Geological Map of Ethiopia*; Scale 1:2,000,000—Ministry of Mines; Geological Survey of Ethiopia: Addis Ababa, Ethiopia, 1996.

15. Geological Survey of Tanzania. Geological and Mineral Information System. 2019. Available online: http://www.gmis-tanzania.com/ (accessed on 9 February 2021).

16. Schlüter, T. *Geological Atlas of Africa*; Springer: Berlin/Heidelberg, Germany, 2006; p. 307.

17. Rosendahl, B.R. Architecture of continental rifts with special reference to East Africa. *Annu. Rev. Earth Planet. Sci.* **1987**, *15*, 445–503. [CrossRef]

18. Braile, L.W.; Keller, G.R.; Wendlandt, R.F.; Morgan, P.; Khan, M.A. The East African rift system. In *Continental Rifts: Evolution, Structure, Tectonics*; Olsen, K.H., Ed.; Elsevier: Amsterdam, The Netherlands, 1995; Volume 25, pp. 213–231.

19. Rooney, T.O. The Cenozoic magmatism of East-Africa: Part I—Flood basalts and pulsed magmatism. *Lithos* **2017**, *286*, 264–301. [CrossRef]

20. Mohr, P.; Zanettin, B. The Ethiopian flood basalt province. In *Continental Flood Basalts*; Macdougall, D.J., Ed.; Kluwer Academic Publishers: Berlin/Heidelberg, Germany, 1988; pp. 63–110.

21. Hofmann, C.; Courtillot, V.; Feraud, G.; Rochette, P.; Yirgu, G.; Ketefo, E.; Pik, R. Timing of the Ethiopian flood basalt event and implications for plume birth and global change. *Nature* **1997**, *389*, 838–841. [CrossRef]

22. Guiraud, R.; Bosworth, W.; Thierry, J.; Delplanque, A. Phanerozoic geological evolution of Northern and Central Africa: An overview. *J. Afr. Earth Sci.* **2005**, *43*, 83–143. [CrossRef]

23. Hayward, N.; Ebinger, C. Variations in the along-axis segmentation of the Afar Rift system. *Tectonics* **1996**, *15*, 244–257. [CrossRef]

24. Baker, B.H. Tectonics and volcanism of the southern Kenya Rift Valley and its influence on rift sedimentation. In *Sedimentation in the African Rifts*; Frostick, L.E., Ed.; Geological Society of London: London, UK, 1986; Volume 25, pp. 45–57.

25. Leat, P.T. Volcanological development of the Nakuru area of the Kenya rift valley. *J. Afr. Earth Sci.* **1991**, *13*, 483–498. [CrossRef]

26. Roessner, S.; Strecker, M.R. Late Cenozoic tectonics and denudation in the Central Kenya Rift: Quantification of long-term denudation rates. *Tectonophysics* **1997**, *278*, 83–94. [CrossRef]

27. Cohen, K.M.; Finney, S.C.; Gibbard, P.L.; Fan, J.X. ICS International Chronostratigraphic Chart 2020/03. International Commission on Stratigraphy, IUGS. 2020. Available online: www.stratigraphy.org (accessed on 9 February 2021).

28. Shackleton, R.M. *Geology of the Nyeri Area*; Technical Report; Ministry of Environment and Natural Resources, Mines and Geological Department: Nairobi, Kenya, 1945; Volume 12, p. 26.

29. Thompson, A.O.; Dodson, R.G. *Geology of the Naivasha Area: Explanation of Degree Sheet 43 S.W*; Ministry of Commerce and Industry, Geological Survey of Kenya: Nairobi, Kenya, 1963; p. 88.

30. Thompson, A.O. *Geology of the Kijabe Area: Degree Sheet 43 S.E. Quarter*; Ministry of Natural Resources, Geological Survey of Kenya: Nairobi, Kenya, 1964; Volume 67, p. 52.

31. McCall, G.J.H. *Geology of the Nakuru—Thomson's Falls—Lake Hannington Area*; Technical Report; Ministry of Environment and Natural Resources, Mines and Geological Department: Nairobi, Kenya, 1967; Volume 3, p. 122.

32. Jennings, D.J. *Geology of the Molo Area, Degree Sheet 42 NE Quarter*; Report; Geological Survey of Kenya: Nairobi, Kenya, 1971; Volume 86, p. 39.

33. Clarke, M.C.G.; Woodhall, D.G.; Allen, D.; Darling, G. *Geological, Volcanological and Hydrogeological Controls on the Occurrence of Geothermal Activity in the Area Surrounding Lake Naivasha, Kenya*; British Geological Survey, Kenia Ministry of Energy: Nairobi, Kenya, 1990; p. 138.

34. Williams, L.A.J. *Geology of the Mau Area*; Technical Report; Ministry of Environment and Natural Resources, Mines and Geological Department: Nairobi, Kenya, 1991; Volume 96, p. 46.

35. Baker, B.H.; Mitchell, J.G.; Williams, L.A.J. Stratigraphy, geochronology and volcano-tectonic evolution of the Kedong–Naivasha–Kinangop region, Gregory Rift Valley, Kenya. *J. Geol. Soc. Lond.* **1988**, *145*, 107–116. [CrossRef]

36. Smith, M. Stratigraphic and structural constraints on mechanisms of active rifting in the Gregory Rift, Kenya. *Tectonophysics* **1994**, *236*, 3–22. [CrossRef]

37. Simiyu, S.M.; Keller, G.R. An integrated geophysical analysis of the upper crust of the southern Kenya rift. *Geophys. J. Int.* **2001**, *147*, 543–561. [CrossRef]

38. Guth, A.L. Spatial and Temporal Evolution of the Volcanics and Sediments of the Kenya Rift. Ph.D. Thesis, Department of Geological and Mining Engineering and Sciences, Michigan Technological University, Houghton, MI, USA, 2013.

39. Crossley, R. The Cenozoic stratigraphy and structure of the western part of the Rift Valley in southern Kenya. *J. Geol. Soc.* **1979**, *136*, 393–405. [CrossRef]

40. Baker, B.H.T.; Wohlenberg, J. Structure and evolution of the Kenya Rift Valley. *Nature* **1971**, *229*, 538–542. [CrossRef] [PubMed]

41. Bergner, A.G.; Strecker, M.R.; Trauth, M.H.; Deino, A.; Gasse, F.; Blisniuk, P.; Duehnforth, M. Tectonic and climatic control on evolution of rift lakes in the Central Kenya Rift, East Africa. *Quat. Sci. Rev.* **2009**, *28*, 2804–2816. [CrossRef]

42. Strecker, M.R.; Blisniuk, P.M.; Eisbacher, G.H. Rotation of extension direction in the central Kenya Rift. *Geology* **1990**, *18*, 299–302. [CrossRef]

43. Williams, L.A.J.; Chapman, G.R. Relationships between major structures, salic volcanism and sedimentation in the Kenya Rift from the equator northwards to Lake Turkana. In *Sedimentation in the African Rifts*; Frostick, L.E., Reault, R.W., Reid, I., Tiercelin, J.J., Eds.; The Geological Society: London, UK, 1986; Volume 25, pp. 59–74.

44. Zielke, O.; Strecker, M.R. Recurrence of large earthquakes in magmatic continental rifts: Insights from a paleoseismic study along the Laikipia-Marmanet Fault, Subukia Valley, Kenya Rift. *Bull. Seismol. Soc. Am.* **2009**, *99*, 61–70. [CrossRef]

45. Leat, P.T. Geological evolution of the trachytic caldera volcano Menengai, Kenya Rift Valley. *J. Geol. Soc. Lond.* **1984**, *141*, 1057–1069. [CrossRef]

46. Leat, P.T. The Structural and Geochemical Evolution of Menengai Caldera Volcano, Kenya Rift Valley. Ph.D. Thesis, University of Lancaster, Lancaster, UK, 1983.

47. Deino, A.L.; Trauth, M.H.; Bergner, A.G.; Potts, R. ^{40}Ar/^{39}Ar Age Calibration of the Lacustrine Sediments at Kariandusi, Central Kenya Rift. In Proceedings of the AGU Fall Meeting Abstracts, San Francisco, CA, USA, 9–13 December 2004.

48. Macdonald, R.; Scaillet, B. The central Kenya peralkaline province: Insights into the evolution of peralkaline salic magmas. *Lithos* **2006**, *91*, 59–73. [CrossRef]

49. Macdonald, R.; Bagiński, B.; Leat, P.T.; White, J.C.; Dzierżanowski, P. Mineral stability in peralkaline silicic rocks: Information from trachytes of the Menengai volcano, Kenya. *Lithos* **2011**, *125*, 553–568. [CrossRef]

50. Wamalwa, A.M.; Mickus, K.L.; Serpa, L.F. Geophysical characterization of the Menengai volcano, Central Kenya Rift from the analysis of magnetotelluric and gravity data. *Geophysics* **2013**, *78*, B187–B199. [CrossRef]

51. Blegen, N.; Brown, F.H.; Jicha, B.R.; Binetti, K.M.; Faith, J.T.; Ferraro, J.V.; Gathogo, P.N.; Richardson, J.L.; Tryon, C.A. The Menengai Tuff: A 36 ka widespread tephra and its chronological relevance to Late Pleistocene human evolution in East Africa. *Quat. Sci. Rev.* **2016**, *152*, 152–168. [CrossRef]

52. Riedl, S.; Melnick, D.; Mibei, G.K.; Njue, L.; Strecker, M.R. Continental rifting at magmatic centres: Structural implications from the Late Quaternary Menengai Caldera, central Kenya Rift. *J. Geol. Soc.* **2020**, *177*, 153–169. [CrossRef]

53. Richardson, J.L.; Richardson, A.E. History of an African rift lake and its climatic implications. *Ecol. Monogr.* **1972**, *42*, 499–534. [CrossRef]

54. Macdonald, R.; Navarro, J.M.; Upton, B.G.J.; Davies, G.R. Strong compositional zonation in peralkaline magma: Menengai, Kenya Rift Valley. *J. Volcanol. Geotherm. Res.* **1994**, *60*, 301–325. [CrossRef]

55. Williams, L.A.J. Character of Quaternary volcanism in the Gregory rift valley. In *Geological Background to Fossil Man: Recent Research in the Gregory Rift Valley, East Africa*; Bishop, W.W., Ed.; Geological Society of London: London, UK, 1978; Volume 6, pp. 55–69.

56. Mboya, B.G.O. Lithostratigraphic Analysis and Palaeoenvironmental Interpretation of the Late Tertiary and Quaternary Sediments of the Nakuru, Elementaita and Navasha Basins. Ph.D. Thesis, Department of Geology, University of Nairobi, Nairobi, Kenya, 1993.

57. Samouëlian, A.; Cousin, I.; Tabbagh, A.; Bruand, A.; Richard, G. Electrical resistivity survey in soil science: A review. *Soil Tillage Res.* **2005**, *83*, 173–193. [CrossRef]

58. Ussher, G.; Harvey, C.; Johnstone, R.; Anderson, E. Understanding the resistivities observed in geothermal systems. In Proceedings of the World Geothermal Congress, Kyushu, Tohoku, Japan, 28 May–10 June 2000; pp. 1915–1920.

59. Yang, X.; Lassen, R.N.; Jensen, K.H.; Looms, M.C. Monitoring CO_2 migration in a shallow sand aquifer using 3D crosshole electrical resistivity tomography. *Int. J. Greenh. Gas Control* **2015**, *42*, 534–544. [CrossRef]

60. Zhou, M.; Wang, J.; Cai, L.; Fan, Y.; Zheng, Z. Laboratory investigations on factors affecting soil electrical resistivity and the measurement. *IEEE Trans. Ind. Appl.* **2015**, *51*, 5358–5365. [CrossRef]

61. Palacky, G.J. Clay mapping using electromagnetic methods. *First Break* **1987**, *5*, 295–306. [CrossRef]

62. Loke, M.H. *Tutorial: 2-D and 3-D Electrical Imaging Surveys*; 2004; p. 136. Available online: www.geoelectrical.com (accessed on 9 February 2021).

63. Loke, M.H. *Tutorial: RES2DINV ver. 3.59, Rapid 2-D Resistivity & IP Inversion Using the Least-Squares Method*; Geotomo Software: Houston, TX, USA, 2010; p. 148.

64. Rikitake, T. Electromagnetic induction within the earth and its relation to the electrical state of the Earth's interior, part I (1). *Bull. Earthq. Res. Inst.* **1950**, *28*, 45–100.

65. Tikhonov, A.N. On determining electrical characteristics of the deep layers of the Earth's crust. *Doklady* **1950**, *73*, 295–297.

66. Cagniard, L. Basic theory of the magneto-telluric method of geophysical prospecting. *Geophysics* **1953**, *18*, 605–635. [CrossRef]

67. Campbell, W.H. *Introduction to Geomagnetic Fields*; Cambridge University Press: Cambridge, UK, 2003.

68. Simpson, F.; Bahr, K. *Practical Magnetotellurics*; Cambridge University Press: Cambridge, UK, 2005; p. 254.

69. Chave, A.D.; Jones, A.G. *The Magnetotelluric Method: Theory and Practice*; Cambridge University Press: Cambridge, UK, 2012.

70. Nakamura, Y. A method for dynamic characteristics estimation of subsurface using microtremor on the ground surface. *Railw. Tech. Res. Institute, Q. Rep.* **1989**, *30*, 25–33.

71. Lermo, J.; Chávez-García, F.J. Site effect evaluation using spectral ratios with only one station. *Bull. Seismol. Soc. Am.* **1993**, *83*, 1574–1594.

72. Bard, P.Y. Microtremor measurements: A tool for site effect estimation. In *The Effect of Surface Geology on Seismic Motion*; Irikura, K., Kudo, K., Okada, H., Sasatani, T., Eds.; Balkema: Rotterdam, The Netherlands, 1999; pp. 1251–1279.

73. Mucciarelli, M.; Gallipoli, M.R. A critical review of 10 years of microtremor HVSR technique. *Boll. Geofis. Teor. Appl.* **2001**, *42*, 255–266.

74. Nakamura, Y. Clear identification of fundamental idea of Nakamura's technique and its applications. In Proceedings of the 12th World Conference on Earthquake Engineering, Auckland, New Zealand, 30 January–4 February 2000; Volume 24, pp. 25–30.

75. Albarello, D.; Cesi, C.; Eulilli, V.; Guerrini, F.; Lunedei, E.; Paolucci, E.; Pileggi, D.; Puzzilli, L. The contribution of the ambient vibration prospecting in seismic microzoning: An example from the area damaged by the 6 April 2009 L'Aquila (Italy) earthquake. *Boll. Geofis. Teor. Appl.* **2011**, *52*, 513–538.

76. Bignardi, S. The uncertainty of estimating the thickness of soft sediments with the HVSR method: A computational point of view on weak lateral variations. *J. Appl. Geophys.* **2017**, *145*, 28–38. [CrossRef]

77. SESAME (Thermal–Hydraulics Simulations and Experiments for the Safety Assessment of Metal Cooled Reactors). *Guidelines for the Implementation of the H/V Spectral Ratio Technique on Ambient Vibrations Measurements, Processing and Interpretation*; SESAME European Research Project—European Commission—Research General Directorate, Project No. EVG1-CT-2000-00026 SESAME; SESAME: Brussels, Belgium, 2004.

78. Mwakirani, R. Exploration of geothermal resources using magnetotellurics case study, Menengay prospect in Kenya. In Proceedings of the Third East African Rift Geothermal Conference, Djibouti City, Djibouti, 22–25 November 2010; pp. 307–316.

79. Nyakundi, E.R.; Githiri, J.G.; Ambusso, W.J. Geophysical Investigation of Geothermal Potential of the Gilgil Area, Nakuru County, Kenya Using Gravity. *J. Geol. Geophys.* **2017**, *6*, 1–10.

80. Sosi, B. Hydraulic Characterization of the Kabatini Aquifer, Upper Lake Nakuru Basin, Kenya rift, Using Geophysical and Pumping Test Data. *Int. J. Dev. Sustain.* **2013**, *2*, 2093–2109.

81. Sosi, B.; Cheboi, E.; Simiyu, C. Nonlinear Correlation analysis between Surface Resistivity and Hydraulic Characteristics of the Kabatini Well Field, Upper Lake Nakuru Basin, Kenya Rift. *IOSR J. Appl. Geol. Geophys.* **2013**, *1*, 35–45. [CrossRef]

82. Flovenz, O.G.; Hersir, G.P.; Saemundsson, K.; Armannsson, H.; Fridriksson, P. Geothermal Energy Exploration Techniques. In *Comprehensive Renewable Energy*; Sayigh, A., Ed.; Elsevier: Amsterdam, The Netherlands, 2012; pp. 51–95.

83. Noor, Y.; Suwai, J.; Kangogo, D. Correlating Resistivity with Temperature and Alteration Mineralogy in Menengai Geothermal Field: Case Study of Menengai Well MW-01. In Proceedings of the 4th African Rift Geothermal Conference, Nairobi, Kenya, 21–23 November 2012; pp. 1–6.

84. Ward, S.H. Resistivity and induced polarization methods. In *Geotechnical and Environmental Geophysics: Volume I, Review and Tutorial*; Ward, S.H., Ed.; Society of Exploration Geophysicists: Tulsa, OK, USA, 1990; pp. 147–189.

85. Bosworth, W.; Strecker, M.; Blisniuk, P. Integration of East African paleostress and present-day stress data: Implications for continental stress field dynamics. *J. Geophys. Res. Solid Earth* **1992**, *97*, 11851–11865. [CrossRef]

86. Bosworth, W.; Strecker, M.R. Stress field changes in the Afro-Arabian rift system during the Miocene to Recent period. *Tectonophysics* **1997**, *278*, 47–62. [CrossRef]